



## Durability of Membrane Electrode Assemblies under Polymer Electrolyte Fuel Cell Cold-Start Cycling

X. G. Yang,<sup>a,\*</sup> Y. Tabuchi,<sup>b</sup> F. Kagami,<sup>b</sup> and Chao-Yang Wang<sup>a,\*</sup>

<sup>a</sup>Electrochemical Engine Center and Departments of Mechanical Engineering and Materials Science and Engineering, The Pennsylvania State University, University Park, Pennsylvania 16802, USA

<sup>b</sup>Nissan Motor Company, Limited, Nissan Research Center, Kanagawa 237-8523, Japan

Electrochemical and microstructural measurements of membrane electrode assemblies (MEAs) cycled under cold-start conditions are reported. An experimental protocol using a single-cell fixture was developed for MEA durability tests under cold-start cycling. Electrochemical diagnostics using high-frequency resistance and pure O<sub>2</sub> found that MEA no. 1 cycled under 100 mA/cm<sup>2</sup> from -30°C does not show any degradation after 100 cycles, MEA no. 2 cycled under 300 mA/cm<sup>2</sup> from -30°C exhibits mild degradation after 150 cycles, and MEA no. 3 cycled under 500 mA/cm<sup>2</sup> from -20°C suffers severe degradation after 110 cycles. Transmission electron microscopy and X-ray diffraction using cross-sectional samples of the aged MEAs further revealed three primary degradation mechanisms: (i) interfacial delamination between the cathode catalyst layer (CL) and membrane, (ii) cathode CL pore collapse and densification upon melting of a fully ice-filled CL, and (iii) Pt particle coarsening and Pt dissolution in perfluorosulfonic acid ionomer. The interfacial delamination and CL densification appear to be closely related to each other, and the key parameter to affect both is the ice volume fraction in the cathode CL after each cold-start step. Eliminating or minimizing these two degradation processes could improve the MEA cold-start durability by 280%. Mitigation strategies, such as improved gas purge prior to cold start, better MEA design, low startup current density, and low cell thermal mass, are proposed. © 2008 The Electrochemical Society. [DOI: 10.1149/1.2926505] All rights reserved.

Manuscript submitted February 3, 2008; revised manuscript received April 15, 2008. Available electronically May 23, 2008.

Durability of polymer electrolyte fuel cells (PEFCs) under dynamic conditions characteristic of automotive applications has received much attention.<sup>1,2</sup> Membrane degradation, platinum dissolution, migration in perfluorosulfonic acid (PFSA) ionomer, and carbon corrosion have all been extensively studied under various operating conditions including high cell potential, high temperatures, high or low humidity, as well as humidity/potential cycling and start/stop operation.<sup>3-11</sup>

Startup of a PEFC from subzero temperatures, commonly referred to as PEFC cold start, is another challenge for automotive applications. Recently, a series of experimental and theoretical studies have clarified the physics governing cold-start performance which led to the development of inraelectrode ice formation (IIF) theory.<sup>12-22</sup> However, little has been reported of the durability of a membrane electrode assembly (MEA) under cold-start cycling, and degradation mechanisms resulting specifically from cold start remain virtually unknown.<sup>12,23,24</sup> McDonald et al.<sup>25</sup> observed that the proton conductivity of Nafion 112 membrane does not change and no degradation in catalyst performance occurs for a dry MEA subjected to freeze/thaw cycling between -40 and -80°C. Wilson et al.<sup>26</sup> showed that freezing at -10°C is not detrimental to the MEA integrity despite its high water content. Cho et al.<sup>27</sup> reported that the performance of a cell containing a proton exchange membrane (PEM) with high water content is degraded after freeze/thaw cycling between -10 and 80°C. However, if the cell is purged with dry gas, almost no performance degradation or increase in membrane resistance can be observed after the freeze/thaw cycling.<sup>28</sup> Guo and Qi<sup>29</sup> showed that freeze/thaw cycles caused the catalyst layer (CL) of a fully hydrated MEA to crack, but freeze/thaw cycles did not lead to apparent damage to the CL if the cell was purged. While there was much controversy in the literature on MEA durability from freeze/thaw cycles and its dependence on the membrane water content, the current consensus is that MEA can survive many hundreds of freeze/thaw cycles between a subzero temperature as low as -40°C and an operating temperature as high as 80°C. Freeze/thaw thermal cycling does not involve net water production in the cathode CL, while subzero startup does involve electrochemical production of water and start/stop effects which impose a harsher condition for MEA

durability. The latter is the subject of the present study. Mao et al.<sup>12</sup> were among the first to study MEA degradation mechanisms resulting from cold start (with water production).

In this work, we first report on our uniquely designed cold-start cycling test protocol. Then, deteriorations in cell performance with cycle number and diagnostics of voltage degradation in terms of kinetic, ohmic, and mass-transport losses are presented. Subsequently, microstructural and chemical changes in aged MEAs are examined by transmission electron microscopy (TEM), scanning electron microscopy (SEM), and X-ray diffraction (XRD) using cross-sectioned MEA samples. Finally, degradation mechanisms specific to cold-start conditions are proposed and discussed.

### Experimental

**MEAs and single-cell fixture.**— For all cold-start durability tests presented in this work, MEAs based on 30 μm fluorinated composite membrane were used, with Pt loading of 0.4 mg/cm<sup>2</sup> (40 wt % Pt/C) at both anode and cathode. The corresponding catalyst layer was about 10 μm in thickness. Carbon paper with a microporous layer was used as gas diffusion layers (GDLs) on both anode and cathode sides. Our cold-start cycling test protocol em-

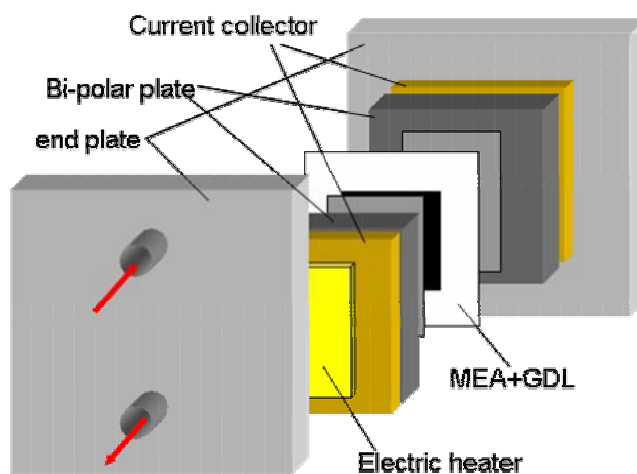


**Figure 1.** (Color online) Schematic of the single-cell fixture used in cold-start cycling tests.

\* Electrochemical Society Active Member.

<sup>c</sup> Present address: Ford Motor Company, Dearborn, MI 48126, USA.

<sup>z</sup> E-mail: cwx31@psu.edu

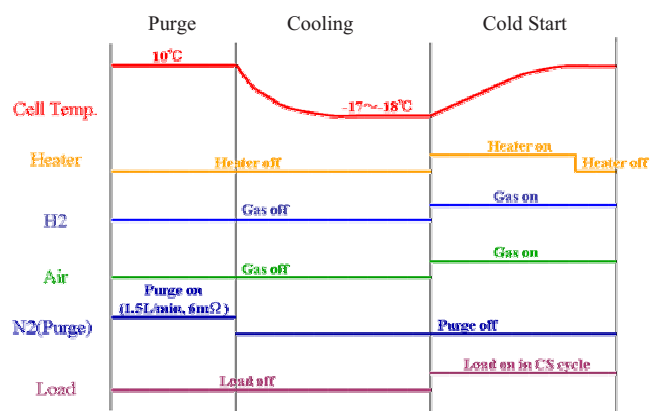


Figure 2. (Color online) Cold-start cycling procedure.

ployed a single cell with active area of 25 cm<sup>2</sup>, as shown in Fig. 1, where bipolar plates were made of graphite with 24 straight channel flow field. In order to mimic the thermal environment of a thin bipolar plate in a fuel cell stack, electric heaters were placed between the current collector and end plate in the present cell fixture as shown in Fig. 1. The use of electric heaters is designed to compensate for the difference in thermal mass between the test fixture and an individual cell in a realistic stack. Assuming adiabatic thermal boundaries, the temperature evolution in realistic cells in a stack environment can be expressed as

$$(mc_p) \frac{dT}{dt} = Q_{\text{gen}} \quad [1]$$

where  $mc_p$  is the thermal mass of the individual cell in a stack, and  $Q_{\text{gen}}$  is the rate of heat generation during cold start originating from entropic heat, irreversible reaction heat, ohmic heat, and latent heat of ice formation.<sup>20,30</sup> Similarly, one can write the thermal balance equation for the single-cell test fixture shown in Fig. 1 such that

$$(mc_p)_{\text{tc}} \frac{dT}{dt} = Q_{\text{gen}} + Q_e \quad [2]$$

where  $(mc_p)_{\text{tc}}$  stands for the thermal mass of the test fixture with a very large heat capacity, and  $Q_e$  is the rate of external heat generation from electric heaters. Obviously, in order to follow the same temperature evolution between the test cell fixture and individual cells in a practical stack, one must have

$$Q_e = \left[ \frac{(mc_p)_{\text{tc}}}{mc_p} - 1 \right] Q_{\text{gen}} = \left[ \frac{(mc_p)_{\text{tc}}}{mc_p} - 1 \right] (E_h - V_{\text{cell}})I \quad [3]$$

where  $E_h$  is the thermal potential ( $=\Delta h/2F \sim 1.48$  V for H<sub>2</sub>-O<sub>2</sub> reaction). The electric heaters were thus controlled according to the cell current and voltage output via Eq. 3. The idea here is simply that the total heat generation (internal plus external) is adjusted to reproduce the same transient thermal environment in a test fixture of much larger heat capacity.

**Cold-start cycling protocol.**— The cycling test protocol is schematically shown in Fig. 2 and the operating conditions are summarized in detail in Table I. Gas purge is usually exercised in automotive fuel cell stacks in order to remove excess liquid water in flow channels and manifolds as well as to prepare for cold start. In the present experiments, gas purge by dry nitrogen was conducted in order to control the initial water condition prior to cold start. Prior to gas purge the fuel cell was operated under 500 mA/cm<sup>2</sup> at 55°C for 15 min and then idled to quickly clean up liquid water in channels and gas lines, followed by natural cooling to 10°C. Nitrogen gas purge was then carried out at both sides at 10°C until the cell's high-frequency resistance (HFR) rose to 150 mΩ cm<sup>2</sup> as monitored by a Tsuruga AC milliohm meter, model 3356 (Tsuruga Electric

Table I. Operating conditions in cold-start cycle tests.

Item	Condition
Gas	Anode H <sub>2</sub> > 99.9999% Cathode air
Temperature	-20°C (500 mA/cm <sup>2</sup> ), -30°C (300 and 100 mA/cm <sup>2</sup> )
Stoichiometric ratio (SR)	Anode SR = 5.0 Cathode SR = 5.0
Current density	100, 300, and 500 mA/cm <sup>2</sup>
Purge condition	Gas: dry nitrogen at both sides Flow rate: 1.5 NL/min Temperature: 10°C
	Duration: until HFR increases to 150 mΩ cm <sup>2</sup>

Corporation, Osaka Japan). In the subsequent cooling stage, the cell temperature was cooled to a prescribed startup temperature (either -20 or -30°C in the present study) in an environmental chamber. When the cell temperature stabilized at the preset startup temperature, a constant current density was imposed on the cell to commence the cold-start stage and at the same time the electric heaters were turned on to compensate for large thermal mass.

**In situ cell diagnostics.**— After a certain number of cold-start cycles, the cell polarization curve was evaluated under the normal operating conditions listed in Table II using a fuel cell testing system illustrated in Fig. 3. The cell HFR was also measured by the Tsuruga milliohm meter. Polarization curves of H<sub>2</sub>/O<sub>2</sub> and H<sub>2</sub>/air along with the HFR data enabled the breakdown of kinetic, ohmic, and mass-transport overpotential. The ohmic voltage loss was estimated from the measured HFR, while the mass-transport loss was estimated from the oxygen gain defined by the difference of IR-corrected voltage between the H<sub>2</sub>/O<sub>2</sub> and H<sub>2</sub>/air polarization curves.<sup>31</sup> Finally, the

Table II. Operating conditions for polarization curve evaluation.

Item	Condition
Gas	Anode H <sub>2</sub> > 99.9999% Cathode: air or pure O <sub>2</sub>
Temperature	70°C
Stoichiometry	Anode SR = 1.5 Cathode SR = 2.5
Relative humidity (RH)	Anode RH: 60% Cathode RH: 50%
Pressure	Ambient (absolute)
Current density	0-1.1 A/cm <sup>2</sup>

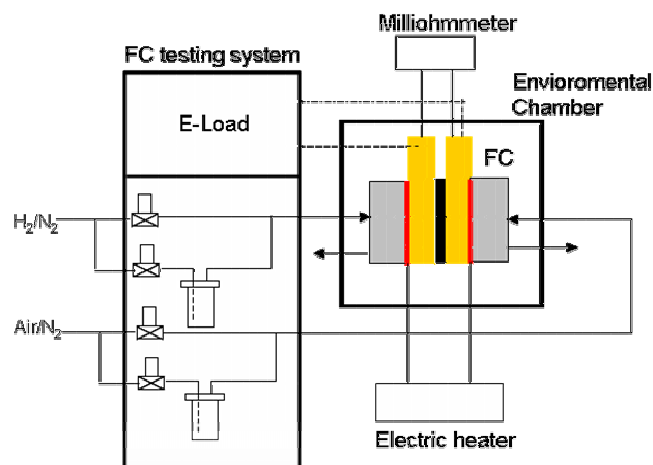


Figure 3. (Color online) Illustration of the testing system.

Table III. Summary of cold-start cycle test results.

	MEA 1	MEA 2	MEA 3
Current density	100 mA/cm <sup>2</sup>	300 mA/cm <sup>2</sup>	500 mA/cm <sup>2</sup>
Temperature	-30°C	-30°C	-20°C
Cycle number	100 cycles	150 cycles	110 cycles
Initial and final $V_{\text{cell}}$ at 1 A/cm <sup>2</sup> and 70°C	No degradation	0.561–0.548 V	0.588–0.257 V
Delamination	No	No	Severe
CL densification	No	Mild	Severe
Pt coarsening	No	Mild	Severe

kinetic loss was evaluated by the voltage difference between the equilibrium potential and IR-corrected voltage with further correction for leak current through the membrane.

**Microstructural and chemical analysis.**— The aged MEAs cycled from the above-described cold-start procedure were examined by TEM and SEM. Ultrathin (~75 nm) cross-sectioned specimens cut from aged MEAs were obtained by resin embedding and ultramicrotomy. The embedding provides specimens with sufficient mechanical strength for subsequent sectioning and also helps retain the structural morphology of electrodes intact after sectioning. An MEA sample was first embedded in Spurr resin (Electron Microscopy Sciences, Fort Washington, PA) for 24 h at 60°C. The low embedding temperature prevents catalyst grain growth and imposes less impact on the CL microstructure. Ultrathin cross sections were cut with glass knives in floating water using a Leica Ultracut E ultramicrotome (Leica, Deerfield, IL) and then transferred to specimen support grids. Preliminary TEM examination indicated that cross-sectional specimens were in excellent condition.

TEM observation was performed with a 200 kV JEOL 2010F field-emission TEM, which was equipped with an annular dark field detector, a postcolumn electron energy loss image (Gatan Enfina), and an Oxford energy-dispersive X-ray (EDX) detector. High angular dark-field scanning TEM (STEM) images and EDX analysis were used to determine the structure and chemical compositions across the MEA. The duration of the EDX scans on individual spots was 5–10 s. In addition, cross-sectional images of MEAs were also obtained using a field-emission scanning electron microscope (JSM-6700F) operated at 1.0 keV. Here, STEM was used specifically to study the change of CL thickness and its densification, high-resolution TEM (HR-TEM) was used to investigate Pt particle growth in an aged CL, and SEM analysis was performed to confirm changes in the CL and membrane thickness. While STEM can also be used to investigate the thickness of CL and membrane, such measurements are often obscured by the cutting angle of microtome used in the preparation of TEM samples. Thus, SEM was conducted in this study in order to obtain more accurate data on the membrane and CL thickness.

XRD was also performed to determine the average Pt size across a MEA based on Scherrer's equation. The average particle size data so determined was used in conjunction with local Pt particle sizes seen by TEM.

### Results and Discussion

**Changes in polarization behavior during durability testing.**— A summary of three MEAs resulting from cold-start cycling is shown in Table III, and their changes in polarization curve are depicted in Fig. 4. It can be seen that MEA no. 1, cycled from -30°C at 100 mA/cm<sup>2</sup> startup current density, experienced virtually no degradation after 100 cycles. When the startup current density increased to 300 mA/cm<sup>2</sup>, MEA no. 2, also cycled from -30°C, suffered a mild degradation of only 13 mV at 1 A/cm<sup>2</sup> after 150 cycles. In contrast, when the current density increased to 500 mA/cm<sup>2</sup> (rapid cold start), MEA no. 3, cycled from -20°C, showed 330 mV degradation at 1 A/cm<sup>2</sup> after 110 cycles. In addition, Fig. 4 shows that the HFR of MEA 3 increased appreciably between 95 and 110 cycles. Clearly, the startup current density is a significant factor

influencing MEA durability resulting from cold start; as such, it represents an important parameter to achieve accelerated durability testing.

**Breakdown of voltage losses.**— A breakdown of degradations in the kinetic, ohmic, and mass-transport overpotential is shown in Fig. 5. For MEAs 1 and 2, a small increase in kinetic loss was observed, and overall the cell performance was minimally degraded. For MEA 3 (500 mA/cm<sup>2</sup>, -20°C, 110 cycles), it is seen from Fig. 5 that there is a 120 mV increase in ohmic loss at 1 A/cm<sup>2</sup>, 77 mV increase in kinetic loss, and 135 mV increase in mass-transport loss. Obviously, MEA degradation comes mainly from ohmic and mass-

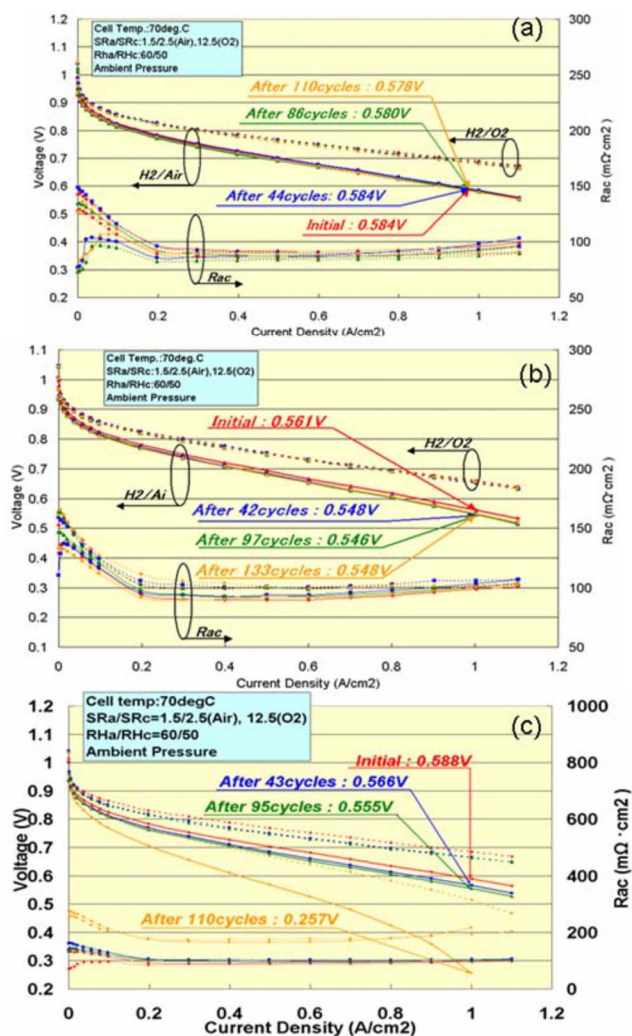
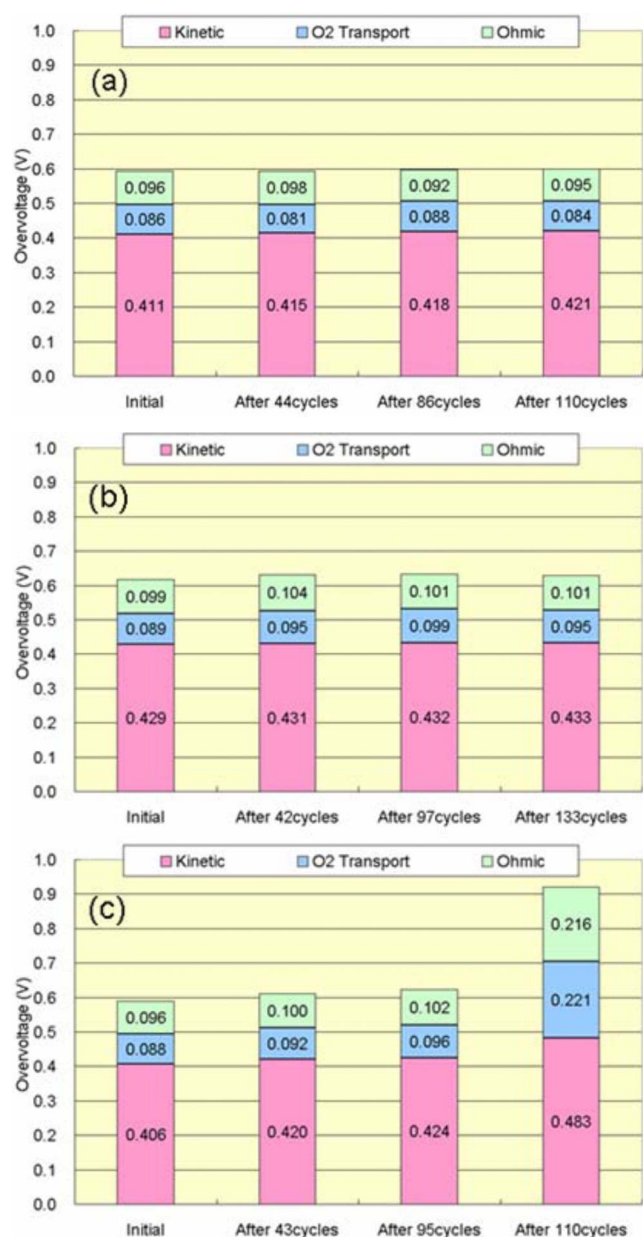


Figure 4. (Color online) Polarization curves after cold-start cycles for (a) MEA 1, (b) MEA 2, and (c) MEA 3 as listed in Table III.



**Figure 5.** (Color online) Results of overpotential breakdown at 1 A/cm<sup>2</sup> and 70°C for (a) MEA 1, (b) MEA 2, and (c) MEA 3.

transport components. Furthermore, it is seen from Fig. 4 that severe degradation started after 95 cycles. Detailed discussion of degradation mechanisms is deferred to a later section.

**Microstructural and chemical changes.**—TEM images of an entire cathode CL of a fresh MEA prior to durability testing are shown in Fig. 6 as a reference. The CL thickness is seen to be around 9 μm, which is consistent with the technical specification of the original MEAs. In addition, there is a tight bonding at the interface between the membrane and cathode CL. The XRD result of the fresh MEA is shown in Fig. 7. Using Scherrer's equation, the Pt particle diameter is determined to be 2.6 nm, in line with TEM observations. However, XRD analysis includes Pt particles both on carbon support and in the ionomer phase, with the latter being electrochemically inactive.<sup>4</sup> Thus, XRD may not be solely used to determine the electrochemically active Pt area in an aged MEA from cold-start cycles where a substantial fraction of Pt may be precipitated in the ionomer phase.

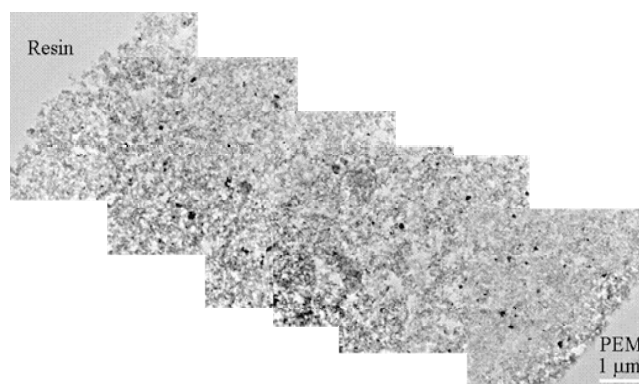


**Figure 6.** (Color online) TEM images of a fresh MEA prior to cold-start cycling.

For brevity, microstructural and chemical analysis results for MEA 1 (100 mA/cm<sup>2</sup>, -30°C, 100 cycles) are not shown here, as this MEA did not show any degradation after 100 cycles. Few selective results are presented here for MEA 2 (300 mA/cm<sup>2</sup>, -30°C, 150 cycles), which experienced only mild degradation. Figure 8a shows a montage of the cathode CL in aged MEA 2. It appears that the aged cathode exhibits a relatively flawless microstructure; however, the interfacial layer within 0.5 μm close to the membrane displays some sign of densification (marked by dark color) and Pt particle coarsening (see Fig. 8b). This may imply that severe degradation is imminent in this MEA after 150 cycles. The anode of this aged MEA 2 is shown in Fig. 9. There is no obvious change in the anode microstructure. High-magnification TEM images shown in Fig. 10 and 11 have captured several long strings of PFSA ionomer in the anode, also indicating that the aged anode remains relatively intact.

Figure 12 contrasts the TEM images of the interfacial regions of the aged cathode to the anode in MEA 2. It is evident that the anode/membrane interface remains a porous structure, while that between the cathode/membrane shows signs of densification. This image, along with a more complete analysis of this aged MEA, indicates that there has not been severe degradation in this MEA; however, the degradation is imminent if given more cycles and will first occur in the cathode CL.

Special attention is paid to analyzing the microstructural and chemical changes occurring in MEA 3 (500 mA/cm<sup>2</sup>, -20°C, 110 cycles) which suffered severe degradation. As mentioned earlier, there was a total of 330 mV degradation in cell performance at 1 A/cm<sup>2</sup>. Moreover, this cold-start cycle (500 mA/cm<sup>2</sup>, -20°C) is interesting as it represents a possible accelerated test protocol for study of MEA degradation resulting from cold start. Figure 13a displays a SEM cross section of the entire MEA 3. It can be seen that the CL thickness ratio is approximately equal to 14:6 between the anode and cathode. Note that the absolute thickness cannot be determined from the image, as the cutting angle of this cross-sectioned sample may not be perfectly normal to the CL in-plane. Assuming that the anode CL remains intact as implied from the above analysis of MEA 2, it can be concluded that the actual anode thickness could remain at ~10 μm while that of the cathode would shrink to only 4.3 μm over 110 cycles. Figure 13b shows an optical micrograph of the aged MEA. The sample was taken from a land area. It is also apparent that the cathode becomes thinner than the anode, consistent with the SEM image shown in Fig. 13a. The darker contrast of the cathode also implies that the cathode CL becomes much denser than the anode. As is explained shortly, the cathode CL shrinkage results from the pore collapse and hence, CL densification, thereby exacerbating the mass-transport loss.

Another distinctive observation of MEA 3 is the interfacial delamination between the cathode CL and membrane, as clearly detected by the low-magnification TEM image shown in Fig. 14.

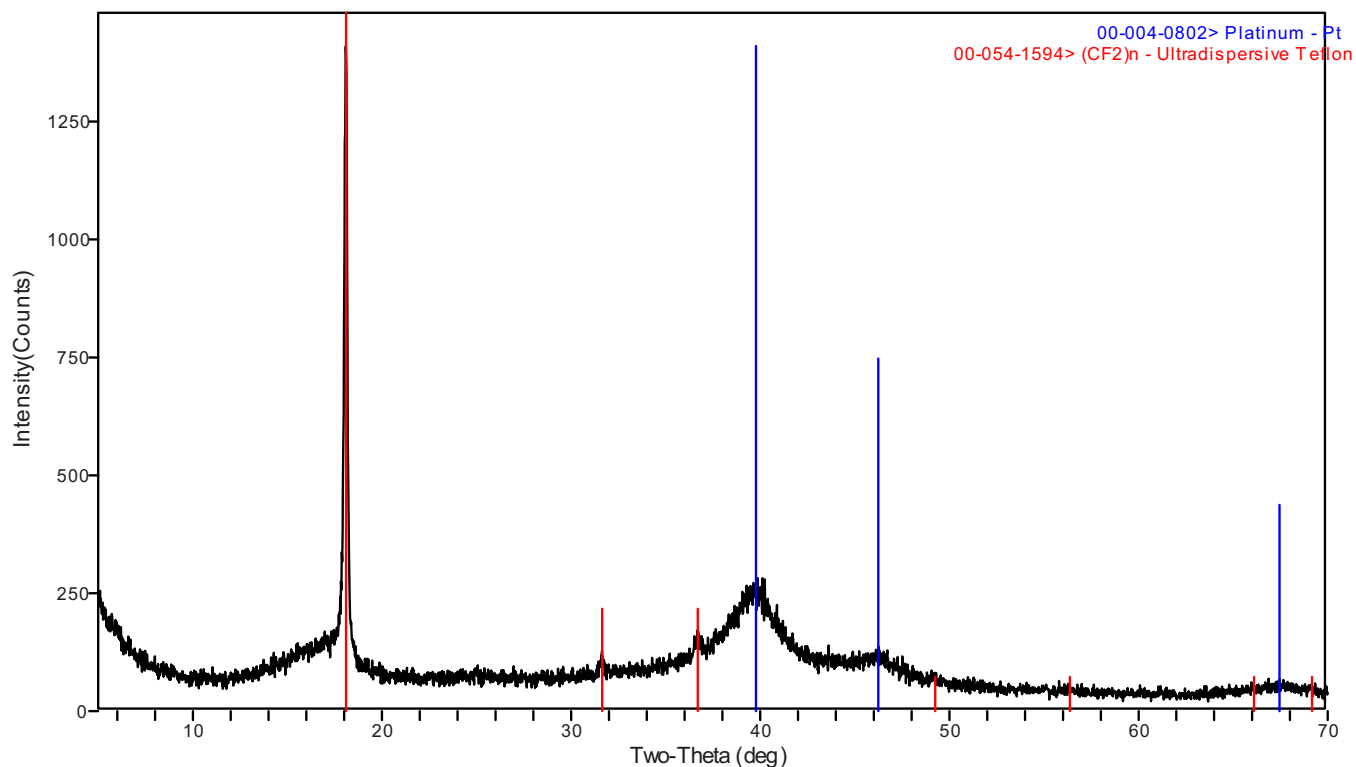


Figure 7. (Color online) XRD patterns of a fresh MEA.

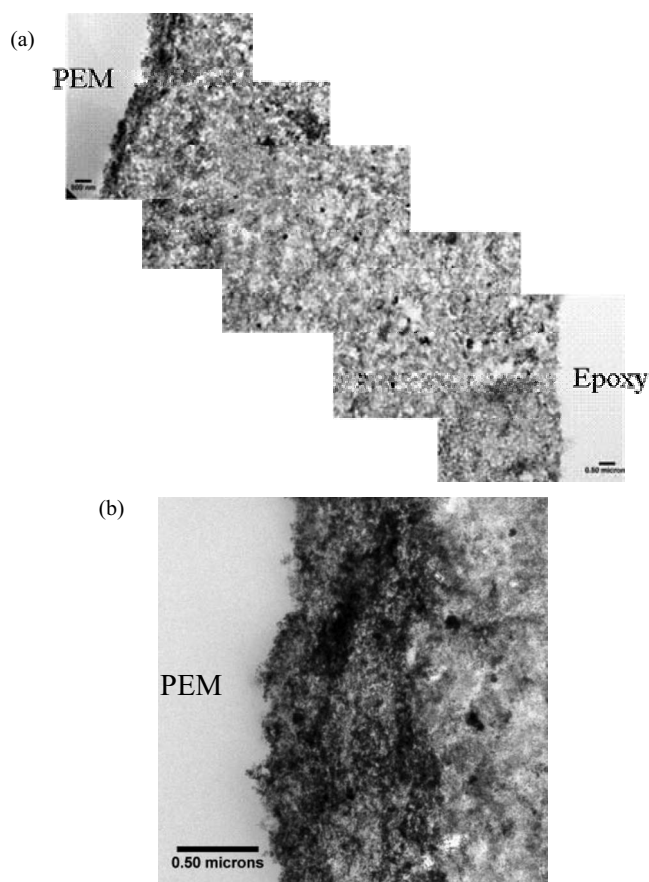


Figure 8. TEM images of aged MEA 2 ( $300 \text{ mA/cm}^2$ ,  $-30^\circ\text{C}$ , 150 cycles) showing (a) the whole cathode catalyst layer and (b) the interface between the membrane and cathode catalyst layer.

The localized delamination is responsible for the increase in ohmic loss of the aged MEA by  $\sim 120 \text{ mV}$ . The interfacial delamination and CL densification appear closely related to each other. Figure 15 shows a montage of TEM images for the aged cathode where the cathode CL is seen to be around  $5 \mu\text{m}$ , confirming the SEM image shown in Fig. 13a. In addition, a gap between the cathode CL and membrane is clearly visible from Fig. 15. Both cathode CL thinning and interfacial delamination originate from cold-start cycling, as they are absent in the fresh MEA.

Aside from the interfacial delamination and CL thinning and densification, MEA 3 also experiences Pt loss, as confirmed by the cyclic voltammograms shown in Fig. 16. It is seen that the Pt area determined by cyclic voltammetry (CV) is significantly reduced over cycles. The other interesting information extracted from these voltammograms is that the double-layer charging current does not change with cold-start cycling, indicating that the area of carbon in contact with ionomer is likely unchanged. This experimental evidence suggests that there is negligible carbon corrosion in cold-start cycling, despite the presence of start/stop, and that the cathode CL thinning may not result from carbon corrosion but from cold start, or more specifically from ice formation during cold start. However,

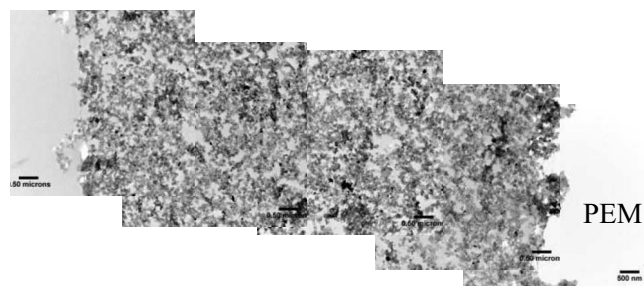
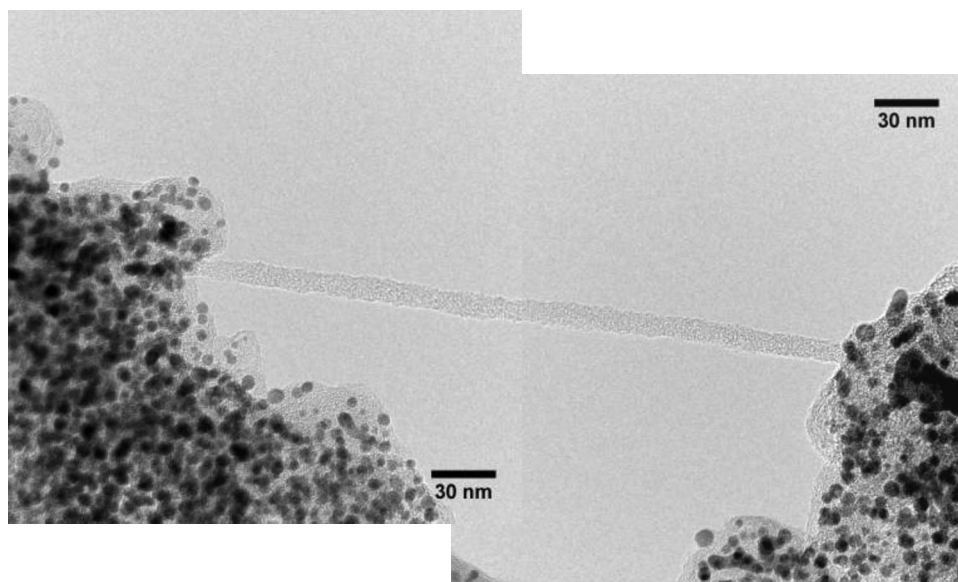


Figure 9. Microstructure of the aged anode in MEA 2 ( $300 \text{ mA/cm}^2$ ,  $-30^\circ\text{C}$ , 150 cycles).

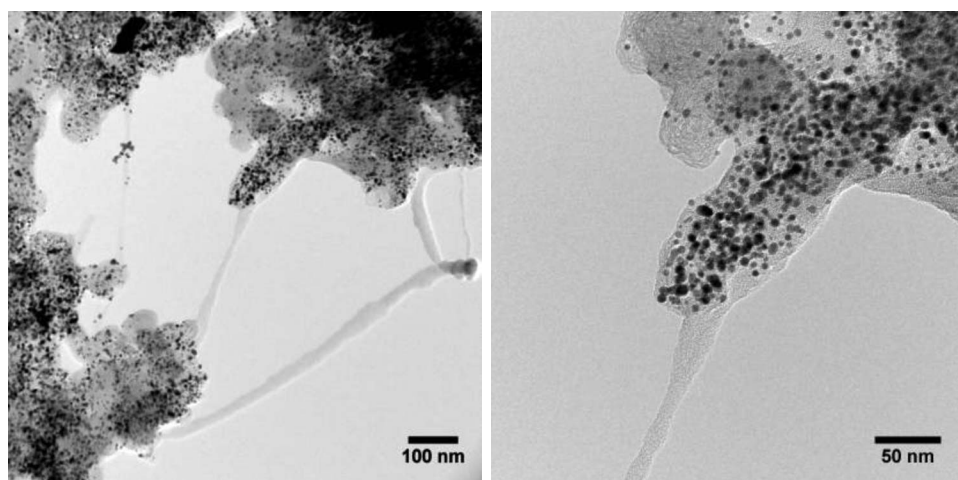


**Figure 10.** A long string of ionomer in the aged anode of MEA 2 close to the membrane, indicating preservation of the anode microstructure.

future research is needed to more clearly separate out carbon corrosion due to start/stop from ice formation and melting in electrodes.

Figure 17 compares TEM images of the fresh cathode with that of the aged cathode in MEA 3. It is found that the size of Pt particles increases from the initial 3 nm to 5–8 nm; this particle growth alone

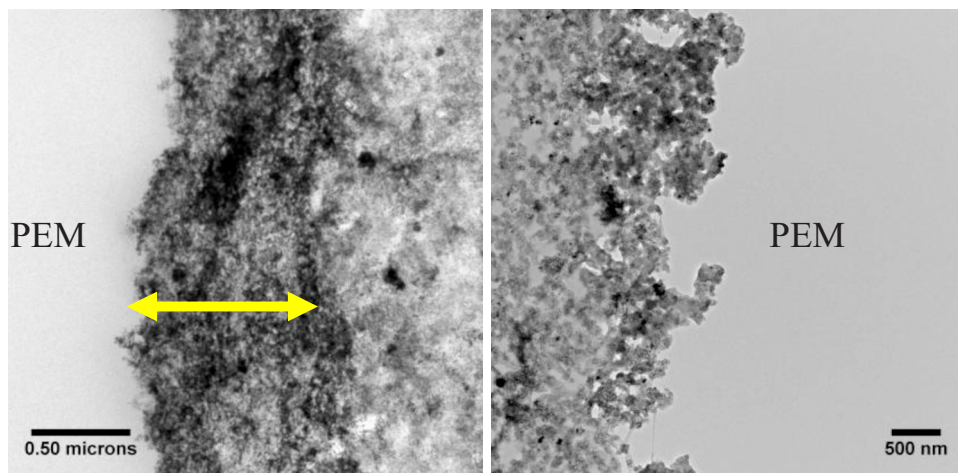
decreases the specific surface area by 50% in the aged cathode. Pt ripening and dissolution in the aged cathode can also be confirmed by XRD. Figure 18 displays the XRD patterns of the aged cathode. A comparison of Fig. 18 with Fig. 7 for the fresh cathode clearly indicates:



Cathode

Anode

**Figure 11.** TEM images of ionomer network in the aged anode of MEA 2 (300 mA/cm<sup>2</sup>, -30°C, 150 cycles).



PEM

PEM

0.50 microns

500 nm

**Figure 12.** (Color online) Comparison of the PEM/CL interfacial regions between aged cathode and anode of MEA 2.

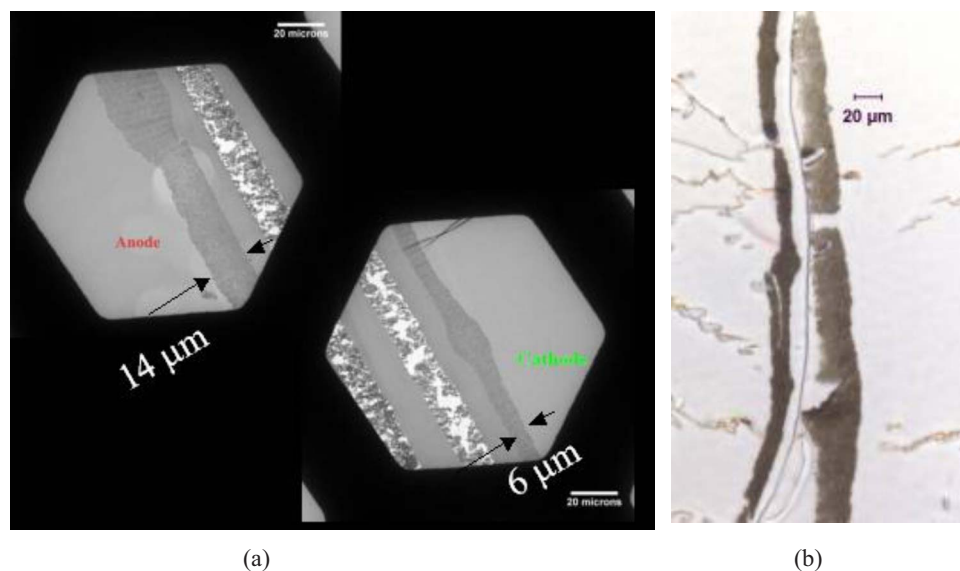


**Figure 13.** (Color online) (a) SEM image of the whole cross section of MEA 3, showing the thickness ratio of the anode (left) to cathode (right) as 6:14, and (b) optical image of the aged MEA cross section with the cathode on the left and anode on the right.

1. The Pt average particle size increases from the initial 2.6 to 4.1 nm after aging.

2. There is no sign of oriented growth for Pt particles in the aged cathode as there is no change in the intensity ratio of Pt peaks.

3. Crystalline poly(tetrafluoroethylene) (PTFE) structure was detected in both samples. It could come from the PTFE-rich backbone microphase in the ionomer/membrane, or from the reinforced porous PTFE inside the membrane. When analyzing the (100) peaks at  $2\theta = 17.991^\circ$ , the PTFE-rich region decreased from 57.1 nm in size to 40.0 nm after aging. This reduction might be due to the degradation of ionomer and hence, fluorine release.

4. Crystallization can be characterized by a crystallinity degree index of Pt, defined by the intensity ratio of  $I_{Pt(111)}/I_{Pt(100)}$ . The intensity ratio increases from 108/942 (0.1146) to 128/727 (0.1761), implying that Pt particles became well-crystallized after aging. It is understandable that smaller Pt particles have a stronger relaxation of surface atoms, causing a deviation from the perfect bulk crystalline structure.

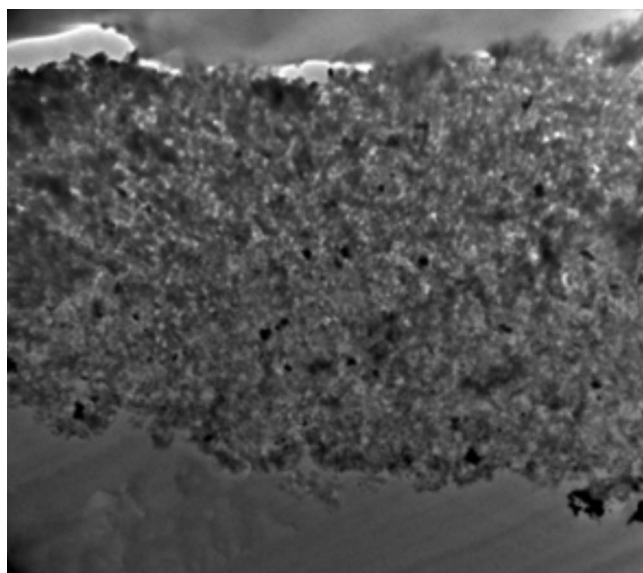


**Figure 14.** Low-magnification TEM image of the cathode CL in MEA 3 showing localized delamination between the CL and membrane.

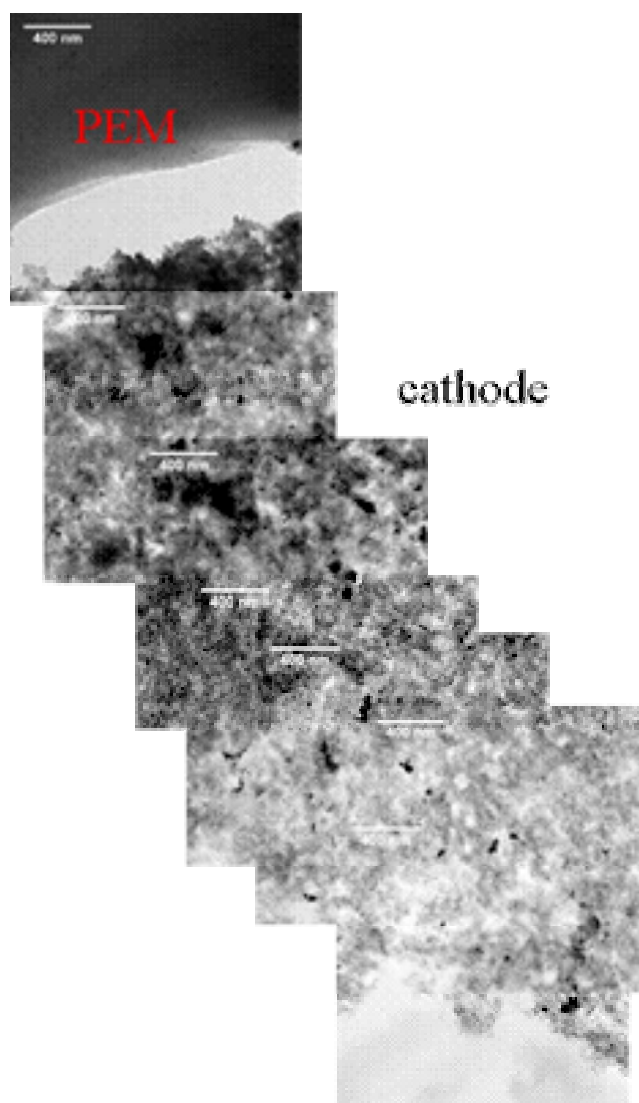


**Figure 15.** (Color online) TEM images of the cathode catalyst layer in aged MEA 3 (500 mA/cm<sup>2</sup>, -20°C, 110 cycles).

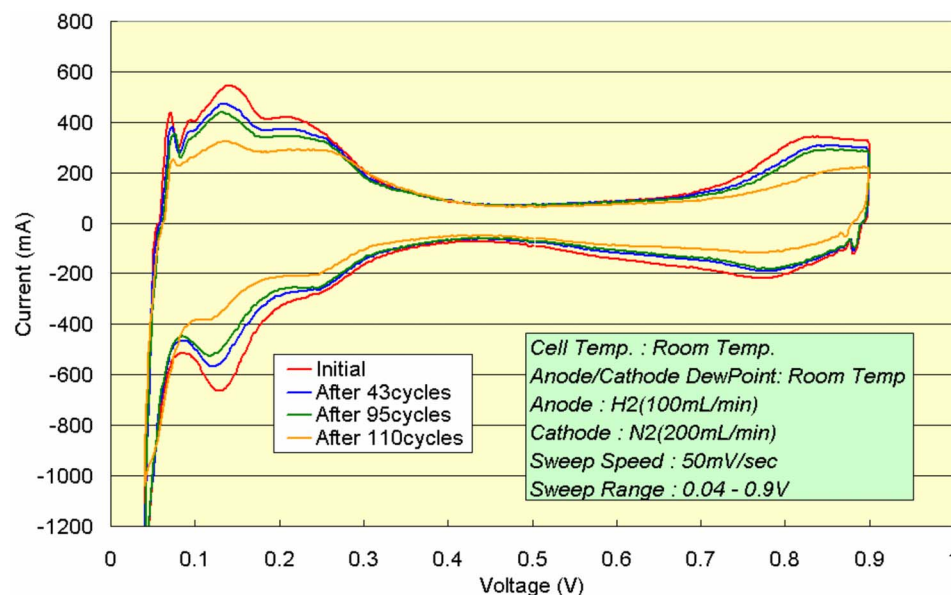


**Figure 16.** (Color online) CV images for MEA 3 ( $500 \text{ mA/cm}^2$ ,  $-20^\circ\text{C}$ , 110 cycles) at various stages of aging.

5. A new peak indicative of carbon is detected in the aged cathode.

6. A slight shift of peak positions is found between two XRD patterns, perhaps due to the unflat surface of the aged cathode.

Note that the X-ray (Cu  $K\alpha$ , 45 keV) used in this XRD study can penetrate inside test samples to a few micrometers, varying with the material property. This means that the signals from the membrane or even the anode may be excited and collected.

Two mechanisms of Pt area loss in normal operation of a PEFC are well-known: Pt particle ripening and Pt dissolution in PFSA ionomer. The kinetics of both are expected to strongly depend on temperature. It is thus surprising to find profound Pt particle growth and dissolution in the ionomer at cold-start conditions. One possible explanation is the large potential swing involved in cold-start cycles which predominantly controls the Pt particle growth and dissolution. The Pt area loss in this aged MEA is responsible for  $\sim 77 \text{ mV}$  kinetic loss after 110 cycles (as confirmed by CV data). When Pt is dissolved in PFSA ionomers and diffused into the membrane where Pt cations are subsequently reduced by crossover hydrogen from the anode, large Pt crystals form inside the membrane. This process clearly takes place in aged MEA 3, as shown in Fig. 19. Based on the above Pt precipitation mechanism, the location of Pt precipitation depends on the diffusivity of Pt ions and  $\text{H}_2$  crossover rate. Under cold-start conditions,  $\text{H}_2$  crossover is retarded, which may cause Pt precipitation to occur on the anode side of the membrane, as detected by the TEM image shown in Fig. 19. In contrast, under normal operation the Pt band is commonly seen close to the cathode

side of the membrane.<sup>4,32,33</sup> Pt deposition near the anode/membrane interface could also be caused by  $\text{H}_2$  starvation in the anode. Further research should be conducted on Pt dissolution and Pt band formation in the membrane under cold-start conditions.

**MEA degradation mechanisms.**— A theory of IIF has emerged from the recent series of experimental and theoretical studies on PEFC cold start.<sup>12-22</sup> This theory states that ice formation in the cathode CL is not only responsible for cell shutdown or startup failure but also dictates the MEA durability from cold-start cycling. The IIF theory has been confirmed by both in situ subzero CV<sup>21</sup> and ex situ cryo-SEM.<sup>19,22</sup> Parameters strongly influencing the amount of ice formed in the cathode include the initial membrane water content (effected by gas purge), startup current density, startup temperature, MEA design, and cell thermal mass. The theory predicts that the higher the startup current density, the more ice formed in the cathode CL. Also, under high current densities, ice distributes more toward the CL/GDL interface.

Based on the IIF theory and the above-described durability test data and microstructural/chemical analysis, we hypothesize three primary mechanisms of MEA degradation occurring in cold start: (i) interfacial delamination between the membrane and cathode CL, (ii) Pt particle growth and Pt dissolution in PFSA ionomer, and (iii) cathode CL structural damage and hence, densification. The first mechanism was also proposed by Cho et al.<sup>28</sup> and Pivovar,<sup>24</sup> but its exact causes and controlling parameters have not been determined. The interfacial delamination is believed to be responsible for the 120 mV increase in ohmic loss in MEA 3, as observed in Fig. 5c, and Pt area loss due to coarsening and dissolution could contribute to the 77 mV increase in kinetic loss. Note that Pt coarsening and dissolution take place under normal cell operation and are not a unique problem of cold start. Therefore, any advances in mitigating Pt area loss under normal operation would benefit MEA durability from cold start as well.

The third degradation mechanism involving CL structural damage and likely densification is responsible for the 135 mV increase in mass-transport loss in MEA 3. CL densification is a plausible explanation for the increased mass-transport loss and is also consistent with the hypothesis of interfacial delamination, because CL densification will most likely leave additional space or partial vacuum in the CL/membrane interfacial region which could peel the CL off the membrane. We hypothesize that the cathode CL thinning and densification results from melting of a completely ice-filled CL. This ice melting results in volume shrinkage, vacuum creation, and finally, pore collapse. In the high-current-density cycling for MEA 3,

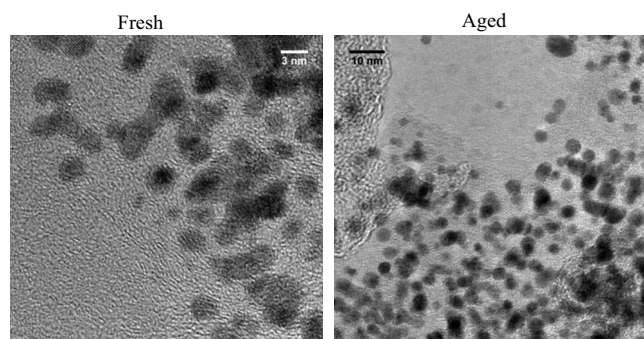


**Figure 17.** Comparison of HR-TEM images of the cathode catalyst layer between fresh MEA and aged MEA 3 ( $500 \text{ mA/cm}^2$ ,  $-20^\circ\text{C}$ , 110 cycles).

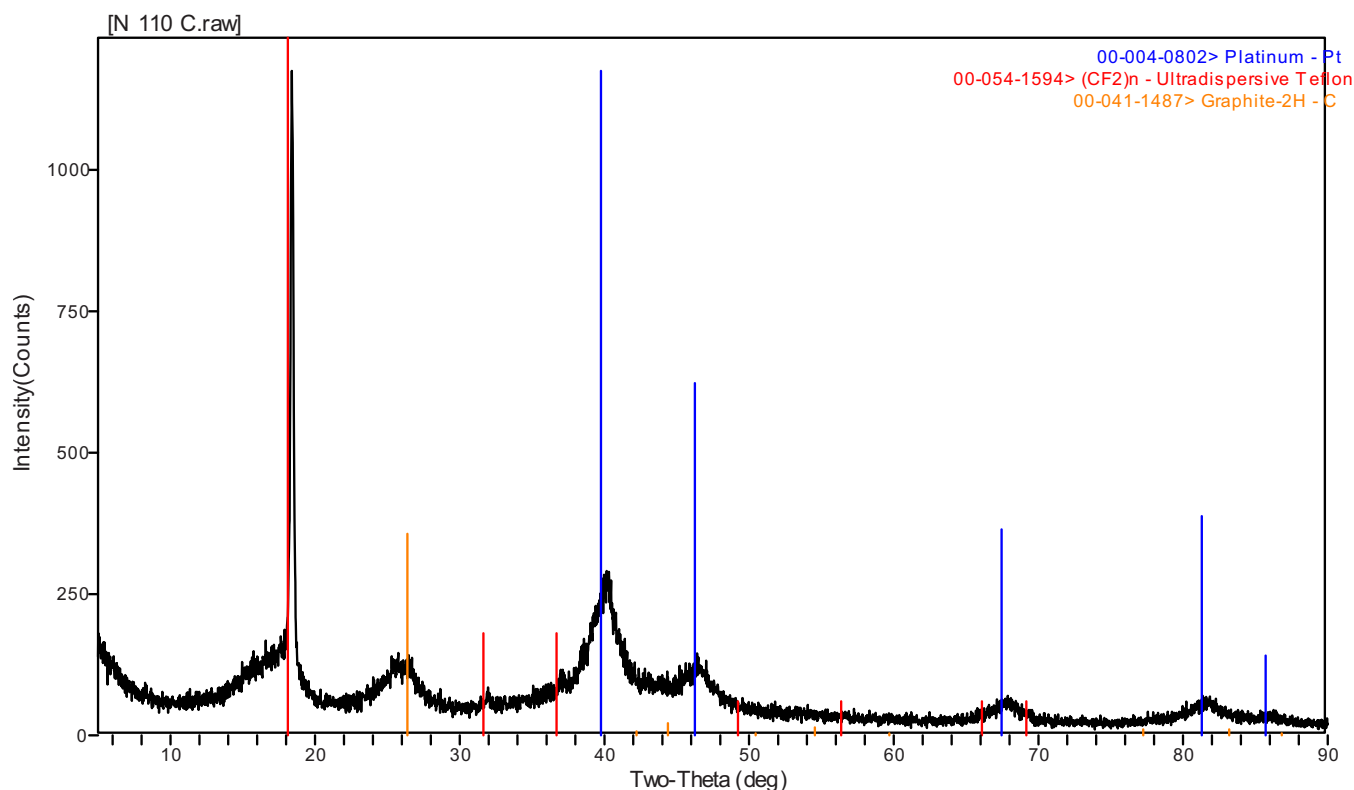


**Figure 18.** (Color online) XRD patterns of the aged MEA 3 ( $500 \text{ mA/cm}^2$ ,  $-20^\circ\text{C}$ , 110 cycles).

most of the product water accumulates in the cathode CL, thereby completely filling it. That is, the volume fraction of ice may have reached nearly 100% of the pore volume. The high ice fraction residing in the cathode CL is then subject to melting once the cell temperature breaks through the freezing point. Melting causes the volume shrinkage and hence, creation of localized vacuum. Local vacuum will exert pressure and stress upon the CL structure. Once

the stress created from vacuum exceeds the integrity pressure of the CL network, the pore structure in CL will partially collapse, thereby resulting in a denser CL. The shrunken CL will also detach from the membrane, causing interfacial delamination. Per this hypothesis, we believe that the CL densification and interfacial delamination are closely related, and solving one problem will avoid the other at the same time.

The mechanism of CL pore collapse and densification also explains why an MEA can sustain many hundreds of freeze/thaw cycles between  $-40$  and  $80^\circ\text{C}$ . During freeze/thaw thermal cycling, there is no net water production and the water or ice level residing in the CL never changes nor reaches close to 100% as long as adequate gas purge is carried out prior to thermal cycling. Therefore, during freezing or melting, there is sufficient open space in the CL porous structure to absorb volume changes without causing CL structural damage.

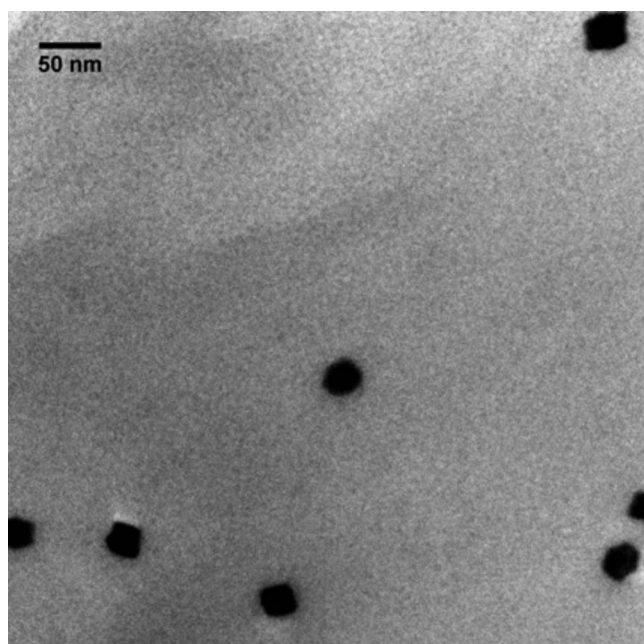


**Figure 19.** TEM image of large, square-shaped Pt crystals on the anode side of the membrane in MEA 3, confirmed by EDX.

*Mitigation strategies of MEA degradation from cold start.*— The key to improving MEA durability from cold start is clearly to mitigate interfacial delamination and CL densification. For MEA 3, this will remove 77 mV ohmic loss and 135 mV mass-transport loss out of a total 330 mV degradation, meaning a 280% improvement in durability. According to the above-presented analysis, a key parameter is the ice fraction in the cathode CL before melting, and a high level should be avoided for improved MEA durability. This suggests that freeze/thaw thermal cycles should incorporate the practice of gas purge. Cold-start cycles should avoid the voltage drop-down period as much as possible. The CV study of Ge and Wang<sup>21</sup> clearly showed that it is in this voltage drop-down period that ice accumulates substantially in the cathode CL (possibly reaching a level close to 100% of all void spaces according to the ex situ cryo-SEM results of Thompson et al.<sup>19</sup> and Li et al.<sup>22</sup>). Known techniques to minimize the ice fraction in the cathode CL and hence, achieve better MEA durability include good purge practice to maintain relatively dry

membranes prior to cold start,<sup>34</sup> low startup current density, high startup temperature, low cell thermal mass, good MEA design, and current ramping with temperature.<sup>35</sup>

### Conclusions

The present study of MEA durability resulting from cold start has found three principal degradation mechanisms: (i) interfacial delamination between the cathode CL and membrane, (ii) cathode CL pore collapse and densification, and (iii) Pt area loss due to particle ripening and dissolution in PFSA ionomer. The interfacial delamination and CL densification are closely tied to each other, and the key parameter to affect both appears to be the ice volume fraction in the cathode CL after each cold start process. If the ice fraction reaches close to 100% of the pore volume in CL, volume extraction upon subsequent ice melting will occur, thereby resulting in localized vacuum and hence, CL pore collapse, CL densification, and interfacial delamination.

It is thus implied that the ability to measure and control the ice fraction inside the cathode CL holds the key to understanding and mitigating the dramatic MEA degradation under harsh cold-start conditions. The subzero CV technique to detect the presence of ice between Pt and ionomer in the CL is a first step in this direction,<sup>21</sup> and more innovative research should be encouraged to develop in situ techniques to measure and monitor the ice amount in the cathode CL.

### Acknowledgments

We acknowledge Nissan Motor Co., Ltd., and Penn State Materials Research Institute (MRI) for financial support of this work and many useful discussions with members of the 2004–2005 ECEC cold-start team when this work was performed. They are Dr. Leng Mao (now at PlugPower), Kazuya Tajiri, Dr. Shanhai Ge, Ankur Gupta, and Dr. Xinhui Ye (now at Spectrum Brands).

The Pennsylvania State University assisted in meeting the publication costs of this article.

### References

- S. D. Knights, K. M. Colbow, J. St-Pierre, and D. P. Wilkinson, *J. Power Sources*, **127**, 127 (2004).
- M. F. Mathias, R. Makharia, H. A. Gasteiger, J. J. Conley, T. J. Fuller, C. J. Gittleman, S. S. Kocha, D. P. Miller, C. K. Mittelsteadt, T. Xie, et al., *Electrochem. Soc. Interface*, **14**, 24 (2005).
- J. Xie, D. L. Wood III, K. L. More, P. Atanassov, and R. L. Borup, *J. Electrochem. Soc.*, **152**, A1011 (2005).
- P. J. Ferreira, G. J. la O', Y. Shao-Horn, D. Morgan, R. Makharia, S. Kocha, and H. A. Gasteiger, *J. Electrochem. Soc.*, **152**, A2256 (2005).
- X. Wang, R. Kumar, and D. J. Myers, *Electrochem. Solid-State Lett.*, **9**, A225 (2006).
- T. Yoda, H. Uchida, and M. Watanabe, *Electrochim. Acta*, **52**, 5997 (2007).
- E. Endoh, S. Terazono, H. Widjaja, and Y. Takimoto, *Electrochem. Solid-State Lett.*, **7**, A209 (2004).
- V. O. Mittal, H. R. Kunz, and J. M. Fenton, *Electrochem. Solid-State Lett.*, **9**, A299 (2006).
- A. Ohma, S. Suga, S. Yamamoto, and K. Shinohara, *J. Electrochem. Soc.*, **154**, B757 (2007).
- B. Sompalli, B. A. Litteer, W. B. Gu, and H. A. Gasteiger, *J. Electrochem. Soc.*, **154**, B1349 (2007).
- C. A. Reiser, L. Bregoli, T. W. Patterson, J. S. Yi, J. D. Yang, M. L. Perry, and T. D. Jarvi, *Electrochem. Solid-State Lett.*, **8**, A273 (2005).
- L. Mao, K. Tajiri, S. Ge, X. G. Yang, and C. Y. Wang, Abstract 998, The Electrochemical Society Meeting Abstracts, Vol. 2005–2, Los Angeles, CA, Oct. 16–21, 2005.
- S. Ge and C. Y. Wang, *Electrochem. Solid-State Lett.*, **9**, A499 (2006).
- L. Mao and C. Y. Wang, *J. Electrochem. Soc.*, **154**, B139 (2007).
- K. Tajiri, Y. Tabuchi, and C. Y. Wang, *J. Electrochem. Soc.*, **154**, B147 (2007).
- L. Mao, C. Y. Wang, and Y. Tabuchi, *J. Electrochem. Soc.*, **154**, B341 (2007).
- K. Tajiri, Y. Tabuchi, F. Kagami, S. Takahashi, K. Yoshizawa, and C. Y. Wang, *J. Power Sources*, **165**, 279 (2007).
- S. Ge and C. Y. Wang, *Electrochim. Acta*, **52**, 4825 (2007).
- E. L. Thompson, J. Jorne, and H. A. Gasteiger, *J. Electrochem. Soc.*, **154**, B783 (2007).
- F. M. Jiang, W. F. Fang, and C. Y. Wang, *Electrochim. Acta*, **53**, 610 (2007).
- S. Ge and C. Y. Wang, *J. Electrochem. Soc.*, **154**, B1399 (2007).
- J. Li, S. Lee, and J. Roberts, Paper 595 presented at the 212th Electrochemical Society Meeting, Washington, DC, Oct. 7–12, 2007.
- J. P. Meyers, *DOE Workshop on Sub-freezing Effects*, U.S. Department of Energy (2005).
- B. Pivovar, *DOE Workshop on Sub-freezing Effects*, U.S. Department of Energy (2005).
- R. C. McDonald, C. K. Mittelsteadt, and E. L. Thompson, *Fuel Cells*, **4**, 208 (2004).
- M. S. Wilson, J. A. Valerio, and S. Gottesfeld, *Electrochim. Acta*, **40**, 355 (1995).
- E. A. Cho, J. J. Ko, H. Y. Ha, S. A. Hong, K. Y. Lee, T. W. Lim, and I. H. Oh, *J. Electrochem. Soc.*, **150**, A1667 (2003).
- E. A. Cho, J. J. Ko, H. Y. Ha, S. A. Hong, K. Y. Lee, T. W. Lim, and I. H. Oh, *J. Electrochem. Soc.*, **151**, A661 (2004).
- Q. Guo and Z. Qi, *J. Power Sources*, **160**, 1269 (2006).
- H. Ju, H. Meng, and C. Y. Wang, *Int. J. Heat Mass Transfer*, **48**, 1303 (2005).
- H. A. Gasteiger, W. Gu, R. Makharia, M. F. Mathias, and B. Sompalli, in *Handbook of Fuel Cells—Fundamentals, Technology and Applications*, W. Vielstich, H. A. Gasteiger, and A. Lamm, Editors, Vol. 3, pp. 593–610, John Wiley & Sons, New York (2003).
- J. Zhang, B. A. Litteer, W. B. Gu, H. Liu, and H. A. Gasteiger, *J. Electrochem. Soc.*, **154**, B1006 (2007).
- W. Bi, G. E. Gray, and T. F. Fuller, *Electrochem. Solid-State Lett.*, **10**, B101 (2007).
- K. Tajiri, C. Y. Wang, and Y. Tabuchi, *Electrochim. Acta*, In press.
- F. M. Jiang and C. Y. Wang, *J. Electrochem. Soc.*, **155**, B743 (2008).